**Title**
Optical Coherence Tomography Elastography Technique for the Early Detections of Osteoarthritis in Rat Articular Cartilage

**Permalink**
https://escholarship.org/uc/item/9v80w1qn

**Author**
Ma, Jonathan Keewon

**Publication Date**
2013

Peer reviewed|Thesis/dissertation

UNIVERSITY OF CALIFORNIA
RIVERSIDE

Optical Coherence Tomography Elastography Techniques for the Early Detections of
Osteoarthritis in Rat Articular Cartilage

A Thesis submitted in partial satisfaction
of the requirements for the degree of

Master of Science

in

Bioengineering

by

Jonathan Keewon Ma

August 2013

Thesis Committee:
      Dr. B. Hyle Park, Chairperson
      Dr. Jin Nam
      Dr. William Grover

The Thesis of Jonathan Keewon Ma is approved:

 

Committee Chairperson

University of California, Riverside

ACKNOWLEDGEMENTS

# TABLE OF CONTENTS

# LIST OF FIGURES

# LIST OF TABLES

# 1. REFERENCES

1. Felson DT, Zhang Y. An update on the epidemiology of knee and hip osteoarthritis with a view to prevention [review]. Arthritis Rheum 1998; 41:1343–55
2. Bijlsma JW, Berenbaum F, Lafeber FPJG. Osteoarthritis: an update with relevance for clinical practice. *Series* 2011; 377: 2115-2126.
3. Dahaghin S, Bierma-Zeinstra SM, Ginai AZ, Pols HA, Hazes JM, Koes BW. Prevalence and pattern of radiographic hand osteoarthritis and association with pain and disability (the Rotterdam study). *Ann Rheum Dis* 2005; 64: 682–87.
4. Oliveria SA, Felson DT, Reed JI, Cirillo PA, Walker AM. Incidence of symptomatic hand, hip, and knee osteoarthritis among patients in a health maintenance organization. *Arthritis Rheum* 1995; 38: 1134–41.
5. Aurich M, Squires GR, Reiner A, et al. Differential matrix degradation and turnover in early cartilage lesions of human knee and ankle joints. *Arthritis Rheum* 2005; 52: 112–19.
6. Goldring MB. The role of the chondrocyte in osteoarthritis. *Arthritis Rheum* 2000; 43: 1916–26.
7. Sellam J, Berenbaum F. The role of synovitis in osteoarthritis. *Nat Rev Rheumatol* 2010; 6: 625–35.
8. Boegard TL, Rudling O, Petersson IF, Jonsson K. Joint space width of the tibiofemoral and of the patellofemoral joint in chronic knee pain with or without radiographic osteoarthritis: a 2-year follow-up. *Osteoarthritis Cartilage* 2003; 11: 370–76.
9. Vignon E, Conrozier T, Hellio Le Graverand MP. Advances in radiographic imaging of progression of hip and knee osteoarthritis. *J Rheumatol* 2005; 32: 1143–45.
10. Abadie E, Ethgen D, Avouac B, et al. Recommendations for the use of new methods to assess the efficacy of disease-modifying drugs in the treatment of osteoarthritis. *Osteoarthritis Cartilage* 2004; 12: 263–68.
11. Regatte RR, Akella SV, Lonner JH, Kneeland JB, Reddy R. T1rho relaxation mapping in human osteoarthritis (OA) cartilage: comparison of T1rho with T2. *J Magn Reson Imaging* 2006; 23: 547–53.
12. Borthakur A, Mellon E, Niyogi S, Witschey W, Kneeland JB, Reddy R. Sodium and T1rho MRI for molecular and diagnostic imaging of articular cartilage. *NMR Biomed* 2006; 19: 781–821.
13. Shapiro EM, Borthakur A, Gougoutas A, Reddy R. 23Na MRI accurately measures fixed charge density in articular cartilage. *Magn Reson Med* 2002; 47: 284–91.
14. Gray ML, Burstein D, Kim YJ, Maroudas A. 2007 Elizabeth Winston Lanier Award Winner. Magnetic resonance imaging of cartilage glycosaminoglycan: basic principles, imaging technique, and clinical applications. *J Orthop Res* 2008; 26: 281–91.
15. Intema F, Thomas TP, Anderson DD, et al. Subchondral bone remodeling is related to clinical improvement after joint distraction in the treatment of ankle osteoarthritis. *Osteoarthritis Cartilage* 2011; published online Feb 12. DOI:10.1016/j.joca.2011.02.005.

16. Wakefield RJ, Gibbon WW, Emery P. The current status of ultrasonography in rheumatology. *Rheumatology (Oxford)* 1999; 38: 195–98.
17. Mancarella L, Magnani M, Addimanda O, Pignotti E, Galletti S, Meliconi R. Ultrasound-detected synovitis with power Doppler signal is associated with severe radiographic damage and reduced cartilage thickness in hand osteoarthritis. *Osteoarthritis Cartilage* 2010; 18: 1263–68.
18. Naredo E, Cabero F, Palop MJ, Collado P, Cruz A, Crespo M. Ultrasonographic findings in knee osteoarthritis: a comparative study with clinical and radiographic assessment. *Osteoarthritis Cartilage* 2005; 13: 568–74.
19. Drexler, Wolfgang, and James G. Fujimoto. *Optical coherence tomography: technology and applications*. Springer, 2008.
20. Wang, Yan, et al. "GPU accelerated real-time multi-functional spectral-domain optical coherence tomography system at 1300nm." *Optics express* 20.14 (2012): 14797-14813.
21. Hee, Michael R., et al. "Polarization-sensitive low-coherence reflectometer for birefringence characterization and ranging." *JOSA B* 9.6 (1992): 903-908.
22. Z. P. Chen, T. E. Milner, D. Dave, and J. S. Nelson, "Optical Doppler tomographic imaging of fluid flow velocity in highly scattering media," Opt. Lett, vol. 22, pp. 64–66, 1997.
23. Morgner, U., et al. "Spectroscopic optical coherence tomography." *Optics letters* 25.2 (2000): 111-113.
24. Chan RC et al. (2004) OCT-based arterial elastography: robust estimation exploiting tissue biomechanics. Opt Express 12: 4558–4572
25. Garra BS, Ce ́spedes EI, Ophir J, Spratt SR, Zuurbier RA, et al. 1997. Elastography of 23. breast lesions: initial clinical results. *Radi- ology* 202:79–86
26. de Korte CL, van der Steen AFW, Ignacio  E, Ce ́spedes EI, Pasterkamp G, et al. 2000. Characterization of plaque components and vulnerability with intravascular ultrasound elastography. *Phys. Med. Biol.* 45:1465– 75
27. Levinson SF, Shinagawa M, Sato T. 1995. Sonoelastic determination of human skele tal muscle elasticity. *J. Biomech.* 28:1145– 27. 54 ment A, Trummer B, Insana MF. 2002. Ac-
28. Adler RS, Rubin JM, Bland PH, Carson PL. 1990. Quantitative tissue motion analy- sis of digitized M-mode images: gestational differences of fetal lung. *Ultrasound Med.* 28. *Biol.* 16:561–69
29. Emelianov SY, Lubinski MA, Skovoroda  AR, Erkamp RQ, Leavey SF, et al. 2000. Reconstructive ultrasound elasticity imag- ing for renal transplant diagnosis: kidney ex-vivo results. *Ultrason. Imag.* 22:178–94
30. Ophir J, Cespedes I, Ponnekanti H, Yazdi  Y, Li X. 1991. Elastography: a quantitative method for imaging the elasticity of biological tissues. *Ultrason. Imag.* 13:111–34
31. Schmitt, Joseph M. "OCT elastography: imaging microscopic deformation and strain of tissue." *Optics express* 3.6 (1998): 199-211.

32. Zhao, Yonghua, et al. "Real-time phase-resolved functional optical coherence tomography by use of optical Hilbert transformation." *Optics Letters* 27.2 (2002): 98-100.

33. Wang, Ruikang K., Sean Kirkpatrick, and Monica Hinds. "Phase-sensitive optical coherence elastography for mapping tissue microstrains in real time."*Applied Physics Letters* 90.16 (2007): 164105-164105.

34. Guzman RE, Evans MG, Bove S, Morenko B, Kilgore K. Monoiodoacetate-induced histologic changes in subchondral bone and articular cartilage of rat femorotibial joints: an animal model of osteoarthritis. *Toxicol Pathol* 2003; 31:619–24

35. Pritzker KP, Gay S, Jimenez SA, Ostergaard K, Pelletier JP, Revell PA, et al. Osteoarthritis cartilage histopathology: grading and staging. Osteoarthritis Cartilage 2006;14:13–29.

36. Nam, Jin, et al. "Transcriptome‐wide gene regulation by gentle treadmill walking during the progression of monoiodoacetate‐induced arthritis." *Arthritis & Rheumatism* 63.6 (2011): 1613-1625.

37. Korhonen, Rami K., and Simo Saarakkala. "Biomechanics and Modeling of Skeletal Soft Tissues." (2011).

38. Keen HI, Lavie F, Wakefield RJ, D'Agostino MA, Hammer HB, Hensor E, Pendleton A, Kane D, Guerini H, Schueller-Weidekamm C, et al. The development of a preliminary ultrasonographic scoring system for features of hand osteoarthritis. Ann Rheum Dis 2008;67:651–655.

39. Qvistgaard E, Torp-Pedersen S, Christensen R, Bliddal H. Reproducibility and inter-reader agreement of a scoring system for ultrasound evaluation of hip osteoarthritis. Ann Rheum Dis 2006;65:1613–1619.

40. Chamberland  D. L., Wang  X., Roessler  B. J., "Photoacoustic tomography of carrageenan-induced arthritis in a rat model," J. Biomed. Opt.. 13, (1 ), 011005  (2008). 1083-3668

41. Wang  X. et al., "Imaging of joints with laser-based photoacoustic tomography: an animal study," Med. Phys.. 33, (8 ), 2691 –2697 (2006). 0094-2405

42. Wang  X., Chamberland  D. L., Jamadar  D. A., "Noninvasive photoacoustic tomography of human peripheral joints toward diagnosis of inflammatory arthritis," Opt. Lett.. 32, (20 ), 3002 –3004 (2007).

43. Sun  Y., Sobel  E. S., Jiang  H., "First assessment of three-dimensional quantitative photoacoustic tomography for *in vivo* detection of osteoarthritis in the finger joints," Med. Phys.. 38, (7 ), 4009 –4017 (2011).

44. Yun SH, Tearney GJ, Bouma BE, Park BH, de Boer JF. High-speed spectral-domain optical coherence tomography at 1.3 um wavelength. Opt Express. 2003; 11 (26): 3598–3604.

45. Park, B., et al. "Real-time fiber-based multi-functional spectral-domain optical coherence tomography at 1.3 μm." *Optics Express* 13.11 (2005): 3931-3944.

# 2. INTRODUCTION/MOTIVATION

Osteoarthritis (OA) is one of the most prevalent chronic joint diseases [1]. Due to the aging population and the outbreak of obesity, the prevalence of osteoarthritis is on the rise [3]. It had been recognized that current diagnostic methods of OA are established late in the disease process and at times too late for any disease-modifying drugs to have any effect [2]. Although many still-imaging procedures and biochemical marker analyses have been developed to monitor the disease, there is a lack of techniques to characterize the mechanical properties of the different layers cartilage impacted by osteoarthritis especially at an early stage [2]. Moreover, a number of elastography methods are destructive. Non-destructive techniques based on ultrasound have been reported in literature, but the inherent resolution limitations makes it difficult to use for assessing the thin layers in a joint. In order to obtain a more accurate definition of OA, this thesis proposes an OCT elastography technique to quantify the progression of tissue stiffness in rat articular cartilage affected by OA.

## 3. BACKGROUND

### 3. 1. OSTEOARTHRITIS (OA)

The presence of OA differs clinically on the site of interest and explicit definition used seen in Table 1 [2]. An OA diagnosis is given in the hand, if 1, 2, 3 or 1, 2, 3, 5 are present. For the hip, an OA diagnosis is given if 1, 2, 4, or 1, 2, 4 or 1, 3, 4. For the knee (clinical and radiographic), an OA diagnosis if 1, 2 or 1, 3, 5, 6, or 1, 4, 5, 6 are present. Finally, knee (clinical), an OA diagnosis is given if 1, 2, 3, 4, or 1, 2, 5, or 1, 4, 5 are present. Radiographs are commonly used to detect OA in patients. Hip, hand, and knee joint space narrowing, subchrondral bone sclerosis, cyst and deformity, and the presences of osteophytes (bony outgrowth associated with degeneration of cartilage) at joint margins characterize radiographic OA. The joint tissues and cartilage of the knee, hip and hand are affected the most and are more prevalent with age. Moreover, OA impacts women over the age of 50 years more than men. In a population-based study by Rottterdam of 3906 people 55 or over, 67% of women had radiographic OA in the hand while 55% of men showed signs of the disease. Additionally, in people older than 80 years; 53% of women and 33% of men had radiographic osteoarthritis of the knee [3]. After age and sex standardization, OA affects 100 per 100,000 person-years of the hand, 88 per 100,000 person-years of the hip, and 240 per 100,000 person-years of the knee [4]. For this thesis, the knee model was selected to be the primary focus for the OCT elastography technique.

**Table 1:** American College of Rheumatology Radiological and Clinical Criteria for OA of the Hand, Knee and Hip.

| Hand (Clinical) | Hip (Clinical and Radiographic) |
|---|---|
| 1. Hand pain, aching, or stiffness for most days of the previous month | 1. Hip pain for most days of previous month |
| 2. Hard tissue enlargement of two or more of ten selected joints* | 2. Erythocyte sedimentation rate of less than 20 mm in the first hour |
| 3. Swelling in two or more metacarpophalangeal joints | 3. Femoral or acetabular osteophytes on radiographs |
| 4. Hard tissue enlargement of two or more distal interphalangeal joints | 4. Hip joint space narrowing on radiographs |
| 5. Deformity of two or more of ten selected | |
| | |
| **Knee (Clinical and Radiographic)** | **Knee (Clinical)** |
| 1. Knee pain for most days of the previous month | 1. Knee pain for most days of the previous month |
| 2. Osteophytes at joint margins on radiographs | 2. Crepitus on active joint motion |
| 3. Synovial fluid typical of OA (Laboratory Test) | 3. Morning stiffness lasting 30 min or less |
| 4. Age 40 or older | 4. Age 38 or older |
| 5. Crepitus on active joint motion | 5. Bony enlargement of the knee on examination |
| 6. Morning stiffness lasting 30 min or less | |

*Ten selected joints include bilateral second and third interphalengael proximal joints, second and third proximal interphaleangeal joints, and first carpometacarpal joint [2].

OA primarily affects the repair process of damaged cartilage due to biomechanical and biochemical changes within the joint. The chondrocytes, cells responsible for maintenance of the extracellular matrix in cartilage, are restricted in its supply of nutrient and oxygen because cartilage is non-vascularized.

During the early stage, crowds of chondrocytes attempt to affect a repair and form in the damaged areas. Additionally, there is a rise in growth factors in the matrix. However, this

attempt fails as OA progresses and the damaged area degrades. The extracellular matrix is unable to withstand normal mechanical stresses due to an increase in the production of tissue-destructive proteinases, an increase in the apoptotic death of chondrocytes, and inadequate production of components of the extracellular matrix. At this point, the tissue enters a dangerous cycle in which the degradation dominates over the synthesis of extracellular matrix. Clinical signs of OA will not be present unless innervated tissues are involved due to the fact that articular cartilage is aneural. This results in one of the reasons for a late diagnosis of OA [5,6].

Even though the physiological processes of OA are primarily cartilage driven, a study by Sellam J. and Berenbaum F. shows an additional and integrated role of synovial tissue and bone and patchy chronic synovitis is apparent [7]. The synovial inflammation corresponds to joint swelling and inflammatory pain, but is considered to be secondary to cartilage debris and catabolic mediators entering the synovial cavity.  As synovial macrophages produce catabolic and pro inflammatory mediators, the balance of cartilage matrix repair and degradation is adversely affected and amplifies synovial inflammation. This happens in both the early and late phases of OA and can be as severe as rheumatoid arthritis adding to the vicious cycle of joint degeneration.

Changes to the subchondral bone such as osteophyte formation, bone remodeling, subchrondral sclerosis and attrition are necessary for radiological diagnosis. These

changes take place not long at the late stages of OA, but also during the beginning, which

suggests subchrondral bone could initiate cartilage damage [8,9].

## 4. PREVIOUS IMAGING METHODS

### 4.1 CLINICAL IMAGING

The gold standard for imaging OA joints is plain radiography. Images under weight-

bearing conditions can be obtained in an inexpensive and quick manner. Although only

calcified bone can be visualized, which only provides an indirect measure of cartilage

thickness and provides no information about synovial tissue. Moreover, imaging

resolutions range from 0.1 to 0.06 mm depending on the focal-spot size, magnification,

and imaging system used As with most clinical imaging modalities, standardization is

implemented. Radiographic grading of OA focuses on osteophyte formation, bone

sclerosis, and joint-space narrowing. While the first two can be seen in the images, joint-

space narrowing can be difficult to quantify as OA progresses as radiography has a

minimum detectable difference of joint-space width of about 0.20 mm with an expected

average annual decrease of about 0.15 mm. Moreover, radiographic images have to be

taken under many imaging sessions to obtain any subtle changes.

Other than radiography, imaging techniques in magnetic resonance imaging (MRI),

computed tomography (CT), and ultrasound have been developed. MRI provides

excellent quantitative morphology of the cartilage and the overall quality and integrity of

the articular cartilage. MRI allows for very sensitive analysis of the volume, area, and

thickness of the knee joint, although some critical limitations are cost, complexity, and time for whole-knee analyses. These limitations inhibit the use of MRI for imaging OA, but it has great value in pinpointing bone marrow and meniscal lesions [10]. Therefore, a number of MRI extensions have been developed to focus on cartilage quality such as T2 MRI is related to collagen orientation and articular cartilage density [11], T1$\rho$ MRI [12], sodium MRI [13], and delayed gadolinium-enhanced MRI [14] provides information about fixed charge density of the cartilage matrix by looking at proteoglycan content. These methods give supplementary information about cartilage quality and can provide information on early changes with the addition of contrast agents [14]. MRI development, unfortunately, is limited by the high cost and long acquisition times and analytical times.

CT images of OA help to provide three-dimensional volume images for further bone characteristic evaluations where traditional radiography cannot, but has very similar disadvantages to radiography with an addition of higher radiation levels. CT has show a convincing relation between dissolving cystic bone area and rain relief after treatment of end-stage OA, but only at resolution in the range of 1 mm [15].

Ultrasound excels in its ability to image soft tissue structures like synovial tissue along all axes without any contrasting agent and allows for the visualization of movement. Besides the critical limitation of imaging depth, ultrasound is quite dependent on user skill and experience especially when visualizing inflammation. [16]. Vascularization of tissues surrounding the knee can be viewed using power doppler ultrasound [17]. Ultrasound

developments are on the rising in the assessment of OA as it is an inexpensive method [18]. Although there have been several studies to introduce a semi quantitative scoring system for osteoarthritis in the knee, hand, and hip joints, no consensus has been reached [38, 39].

Imaging methods that combine both optical and ultrasonic properties are acousto-optics and photoacoustics. Acousto-optic imaging reveals optical properties in the millimeter range in a scattering sample by tagging the photon path with an ultrasonic beam. A focused ultrasound beam is applied to the sample and the crossed effect of light and sound is detected. Since the ultrasound beam typically undergoes no scattering, the acousto-optic signal is linked to the optical properties of the sample within the ultrasound beam. Photoacoustics is an emerging technique for imaging and has been applied to imaging finger joints [42]. Photoacoustic imaging combines optical and laser-induced thermoelastic expansion within a sample tissue. Studies in the rat tail and human OA finger joints demonstrate photoacoustic imaging in achieving sub millimeter resolution and variations induced by inflammation [38, 39, 40, 41]. However, the system compactness, imaging speed, and repeatability of imaging finding limits the adaptation of photoacoustic imaging of OA to a clinical setting [43]. While both techniques use a combination of optical and ultrasonic waves, each technique is a non-destructive imaging modality, as the short laser pulses do not cause any thermal expansion.

# 5. THEORY

## 5.1 FOURIER DOMAIN OPTICAL COHERENCE TOMOGRAPHY (FD-OCT)

Optical Coherence Tomography (OCT) a rising optical imaging modality in the medical imaging community. OCT is analogous to ultrasound, but uses laser light instead of sound waves. It is an interferometric technique capable of high-resolution cross-sectional imaging of biological microstructures by measuring backscattered light. OCT is advantageous, because images are obtained in real time, *in situ*, one to two orders of magnitude finer than conventional ultrasound, non-invasively. OCT Images are similar to histology in geometry and scale without the need to exact, stain, or process the sample [19]. Additionally, OCT imaging can be accelerated through the use of graphical processing units (GPU) [19]. These unique advantages and the rise in development of OCT extensions such as polarization sensitive OCT (PS-OCT) [21], Doppler OCT [22], spectroscopic OCT [23], and optical coherence elastography (OCE) [24], OCT is a promising multi-functional imaging modality for both research and clinical applications.

OCT obtains cross-sectional images by capturing multiple axial measurements of time delay (axial scans, A-scans, A-lines) and scanning the incident optical beam transversely. Two-dimensional data sets are produced, which represent the backscattered light in a cross-sectional plane from the imaging sample. The B-scans or images are then displayed in grey scale or a false color map revealing the imaging sample's structure. Acquiring

sequential B-scans and scanning the incident optical beam in a raster pattern can generate

three-dimensional images volume data sets [19].

## 5.2 POLARIZATION-SENSITIVE OCT (PS-OCT)

PS-OCT can be used to increase contrast by determining a sample birefringence,

diattenuation, and optic axis orientation. Birefringent materials are characterized if the

real part of its refractive index is polarization state dependent. A difference in the

imaginary portion of the refractive index leads to a differential attenuation of polarization

states. Samples displaying this quality are said to be dichroic. However, in biological

tissue, birefringence can be accurately estimated without considering diattenuation [19].

Articular cartilage can be divided in to four zones based on the arrangement of collagen

fibril network. The first and topmost is the superficial zone, where the chondrocytes are

flattened and aligned parallel to the cartilage surface. The collagen fibrils are thin in size

and are parallel to each other. In this layer the water content is the highest and the

proteoglycan content is the lowest. The next layer is the middle zone, where the collage

fibrils are a bit larger in diameter and orient randomly. The water content and cell density

is lower, but the proteoglycan content is higher than the superficial zone. The next zone is

the deep zone, where the collagen fibrils are the largest and are oriented perpendicular to

the articular surface. The cell density and water contents are the lowest while the

proteoglycan content at its highest. The last layer is the calcified cartilage, which

connects the deep zone and the subchondral bone [37]. The distinct orientation changes in

the articular cartilage will cause a difference in the refractive index between layers and can be visualized with PS-OCT.

## 5.3 ELASTOGRAPHY

Ophir et al spearheaded the first ultrasound-based tissue elastography for biomechanical strain imaging in 1991 [30]. Under static condition, Ophir et al formed strain images using external compression methods. Image tissue deformation in large fields became possible as the stress field applied to the body could now be controlled. Medical applications such at tumor detection [25], vascular plaques [26], skeletal muscle contraction [27], fetal lung maturity [28], and renal transplant rejection [29] were researched as the field of elastography grew. Common approached to static elastography today use an external stress stimulus applied thorough an imaging transduce or vascular balloon.

In 1998, Schmitt et al develop OCT elastography by tracking the speckle motion between successive B-scans and showed internal tissue deformations as small as a few microns [31]. Later in 2004, R.C. Chan et al developed an OCT based elastography technique of tissue velocity and strain estimation incorporating prior knowledge of the tissue biomechanics within a variational energy formulation. The approach is based on correlation maximization and provides accurate velocity estimates with low root mean square (RMS) velocity error [24].

## 5.4 PHASE-SENSITIVE OCT ELASTOGRAPHY

An alternate approach to measure tissue deformation is to use the phase information that OCT captures. It is similar to phase-resolved Doppler OCT [32], where the phase changes between consecutive A scans are used to determine the tissue Doppler shifts, except from these phases changes localized deformations are captured. The calculations are shown the next section below.

## 5.5 INTENSITY, PHASE, VELOCITY, & STRAIN RATE CALCULATIONS [18]

In SD-OCT, a line scan camera spectrally resolves the interference signal between the reference and backscattered light from a sample. The spectral encoded outputs from the cameras can be expressed as

$$I(k) = I_r(k) + 2\sqrt{I_s(k)I_r(k)} \sum_n \alpha_n \cos(k\, z_n) + I_s(k) \quad (1)$$

where $I_s(k)$ and $I_r(k)$ are the wavelength-dependent intensities from the sample and the reference arm, respectively and $k$ represents the wavenumber. The interference between the reference and the sample is the second term in (1) ,$2\sqrt{I_s(k)I_r(k)} \sum_n \alpha_n \cos(k\, z_n)$. $\alpha_n$ is square root of the sample reflectivity at depth $z_n$. Depth information from the scatterers in the sample is obtained by taking the inverse Fourier transform of (1), $|FT^{-1}[I(k)]|^2$.

After taking the inverse Fourier transform of *I(k)*, a complex function is generated, where the amplitudes are used to create intensity images, and the phase, $\phi$, is captured shown in equation (2).

14

$$FT^{-1}[I_D(k)] = Re\widetilde{I_D}(z) + jIm[\widetilde{I_D}(z)] = \widetilde{I_D}(z) * \exp[j\phi(z)] \qquad (2)$$

Equations (3) and (4) show how the intensities and the phase can be resolved.

$$Intensity, I_D(l) = \sqrt{Re^2 I_D(z) + Im^2[I_D(z)]} \qquad (3)$$

$$Phase, \phi(z) = arctan\left(\frac{Im\widetilde{I_D}(z)}{Re\widetilde{I_D}(z)}\right) \qquad (4)$$

Intensities are calculated by taking the square root of the real and imaginary parts squared and the depth-resolved phase can be determined by taking the arctangent of the imaginary over the real parts. Although the phase is generally random, it is fixed for the static scatters at the position (x, z), where x is the a-scan and z is the depth. The instantaneous distance, $\Delta z$, displacement of a scatters during a time interval, $\Delta t$, between two successive A-lines will produce a localized change in phase, $\Delta\phi$ of the reflected light, shown in equation 5.

$$\Delta\phi = \frac{4\pi\Delta z}{\lambda_c} \qquad (5)$$

where $\lambda_c$ is the center wavelength of the light source. It is important to remember that the phase is wrapped within a $(-\pi, \pi)$ radian range, because all complex numbers have a unique phase with respect to $2\pi$. The unwrapped phase changes can be determined using phase-unwrapping algorithms.

Therefore, localized velocities in the beam direction can be determined, shown in equation (6).

$$v = \frac{\Delta\phi\lambda_c}{4\pi\Delta t} \qquad (5)$$

where time between successive profiles is $\Delta t = \dfrac{1}{f_{CCD}}$ and $f_{CCD}$ is the frame rate of the line scan camera. The correlation between the phase measurements of successive scans is well

15

preserved, normally. From the depth-resolved instantaneous translation and velocity, the instantaneous strain, $\varepsilon$, and strain rates, $\varepsilon'$, can be determined to quantify the local response of the tissue to a compressive force shown in equations (6) and (7).

$$\varepsilon' = \frac{\Delta\phi\lambda_c}{4\pi z_0 \Delta t}, \quad (6)$$

$$\varepsilon = \frac{\Delta\phi\lambda_c}{4\pi z_0}, \quad (7)$$

where $z_0$ is the initial thickness of the sample at the lateral position before the sample deforms. The strain rate, a temporal derivative of the strain, is a measure of the rate of deformation. A negative strain rate corresponds to the tissue segments shortening or becoming thinner, while a positive strain rate is equivalent to the segment becoming longer or becoming thicker. [18].


## 5.6 ULTRASOUND MODULATED INTENSITY

Starting from the instantaneous power as a function of wavenumber as read on a spectrometer for a retroreflector at a given position z,

$$P(z) = \alpha\cos(kz) \quad (8)$$

Then the intensity for a given line scan camera acquisition time T for a retroreflector at $z_0$ is given by

16

$$I_0(k,z_0) = \int_0^T P(z_0)dt$$
$$= \int_0^T \alpha \cos(kz_0)dt \qquad (9)$$
$$= \alpha \cos(kz_0)t\big]_0^T$$
$$= T\alpha \cos(kz_0)$$

Now assume that the position of that retroreflector is modulated by a high frequency ultrasound modulation such that the position of the retroreflector is now given by

$$z(t) = z_0 + z_1 \cos(\omega t) \qquad (10)$$

Then the ultrasound modulated intensity can be determined as

$$I(k,z) = \int_0^T \alpha \cos\big(k(z_0 + z_1 \cos(\omega t))\big)dt$$
$$= \int_0^T \alpha \cos(kz_0 + kz_1 \cos(\omega t))dt \qquad (11)$$
$$= \int_0^T \alpha\big(\cos(kz_0)\cos(kz_1 \cos(\omega t)) - \sin(kz_0)\sin(kz_1 \cos(\omega t))\big)dt$$

If we assume that, $kz_1 \ll 1$ then the following approximations to the previous equation

$$\cos(kz_1 \cos(\omega t)) = 1 - \tfrac{1}{2}(kz_1 \cos(\omega t))^2 \qquad (12)$$

$$\sin(kz_1 \cos(\omega t)) = kz_1 \cos(\omega t) = 1 \qquad (13)$$

17

$$I(k,z) = \int_0^T \alpha \left( \left( 1 - \tfrac{1}{2}\left( kz_1 \cos(\omega t) \right)^2 \right) \cos(kz_0) - \left( kz_1 \cos(\omega t) \right) \sin(kz_0) \right) dt$$

$$= \int_0^T \alpha \left( 1 - \tfrac{1}{2}\left( kz_1 \cos(\omega t) \right)^2 \right) \cos(kz_0) dt$$

$$= \int_0^T \alpha \cos(kz_0) dt - \int_0^T \alpha \left( \tfrac{1}{2}\left( kz_1 \cos(\omega t) \right)^2 \right) \cos(kz_0) dt$$

$$= T\alpha \cos(kz_0) - \tfrac{1}{2}\alpha k^2 z_1^2 \cos(kz_0) \int_0^T \cos^2(\omega t) dt$$

$$= T\alpha \cos(kz_0) - \tfrac{1}{2}\alpha k^2 z_1^2 \cos(kz_0) \int_0^T \tfrac{1}{2}\left( 1 + \cos(2\omega t) \right) dt \qquad (14)$$

$$= T\alpha \cos(kz_0) - \tfrac{1}{4}\alpha k^2 z_1^2 \cos(kz_0) \int_0^T 1 + \cos(2\omega t) dt$$

$$= T\alpha \cos(kz_0) - \tfrac{1}{4}\alpha k^2 z_1^2 \cos(kz_0) \left( t + \tfrac{1}{2\omega}\sin(2\omega t) \right) \Big]_0^T$$

$$= T\alpha \cos(kz_0) - \tfrac{1}{4}\alpha k^2 z_1^2 \cos(kz_0) \left( T + \tfrac{1}{2\omega}\sin(2\omega T) \right)$$

$$= T\alpha \cos(kz_0) - \tfrac{1}{4}T\alpha k^2 z_1^2 \cos(kz_0) - \tfrac{1}{8\omega}\alpha k^2 z_1^2 \cos(kz_0) \sin(2\omega T)$$

Since $\omega \gg 1$ and $kz_1 \ll 1$, this expression can be further reduced to

$$I(k,z) = T\alpha \cos(kz_0) - \tfrac{1}{4}T\alpha k^2 z_1^2 \cos(kz_0)$$
$$= T\alpha \cos(kz_0)\left( 1 - \tfrac{1}{4}k^2 z_1^2 \right) \qquad (15)$$

Then the ratio of the intensity with and without the effect of ultrasound modulation is given by

$$\frac{I(k,z)}{I_0(k,z_0)} = \frac{T\alpha \cos(kz_0)\left( 1 - \tfrac{1}{4}k^2 z_1^2 \right)}{T\alpha \cos(kz_0)} \qquad (16)$$
$$= 1 - \tfrac{1}{4}k^2 z_1^2$$

Ideally, a convolution could be performed to determine the effect of this reduction in modulation (due to the dependence on k), but to a first approximation. However, we can assume that since the range of wavenumber is relatively small compared to the average wavenumber, the reduction in intensity in the transformed depth profile is given by

$$\frac{I_{US}(z)}{I(z)} = 1 - \tfrac{1}{4}k_{avg}^2 z_1^2 \qquad (17)$$

where $z_1$ is the amplitude of the positional modulation caused by the ultrasound transducer. Since the modulation amplitude is inversely related to the mechanical stiffness of a sample, this reduction in intensity can be used to assess the relative mechanical stiffness of the sample.

This is all under the assumption that the ultrasound frequency is high, and that this frequency is faster than the acquisition rate of the OCT system.

## 6. EXPERIMENTAL APPROACH & ANALYSIS

### 6.1 MULTIFUNCTIONAL SPECTRAL DOMAIN OCT SYSTEM (MF-SD-OCT)

A graphic of the multi-functions SD-OCT system is show in Fig 1. The broadband laser

source is comprised of two super-luminescent diodes (SLD), where one is centered at

1295 with a full-width at half maximum (FWHM) bandwidth of 97nm (Thorlabs Inc.)

and the next is centered at 1350nm with a FWHM bandwidth of 48nm (Denselight

Semiconductors Pte Ltd). This results in a light source centered at 1298 nm with a

FWHM bandwidth of 120nm and 16mW power. The laser light from the source is

collimated and passed through a polarization beam splitter (pb) and a polarization

modulator (pm, Thorlabs Inc.) that switches between the orthogonal polarization states in

a Poincare sphere representation. The polarized light is then passed though a fiber

circulator (Thorlabs Inc.) and an 80/20 fiber splitter (AC Photonics Inc) with a

polarization controller (pc). A neutral density filter is used in the reference arm to insure

uniformity of the reference polarization state. Two galvanometer-mounted mirrors in the

sample arm provide transverse scanning of a 23.4-micron diameter focused spot. Light is

collected from both the sample and reference and combined at the splitter and then passes

through a transmission diffraction grating (1100 lines per mm, Wasatch Photonics) before

being focused by a planoconvex lens. The two polarization states of light are separated by

a polarization beam splitter, and collected by two line scan cameras (Isc, Goodrich SUI

SU-LDH linear digital high speed InGaAs camera) separately with capturing speeds up to

45kHz. National Instruments PCIeNI-1429 boards, then, digitize the output signal. A

synchronized signal from the computer via the National Instruments PCIe6259 board

triggers the cameras, galvanometer mirrors and polarization modulator. The GPU

processes the data for display via PCI express 2.0 x16 interface. The computer is an Intel
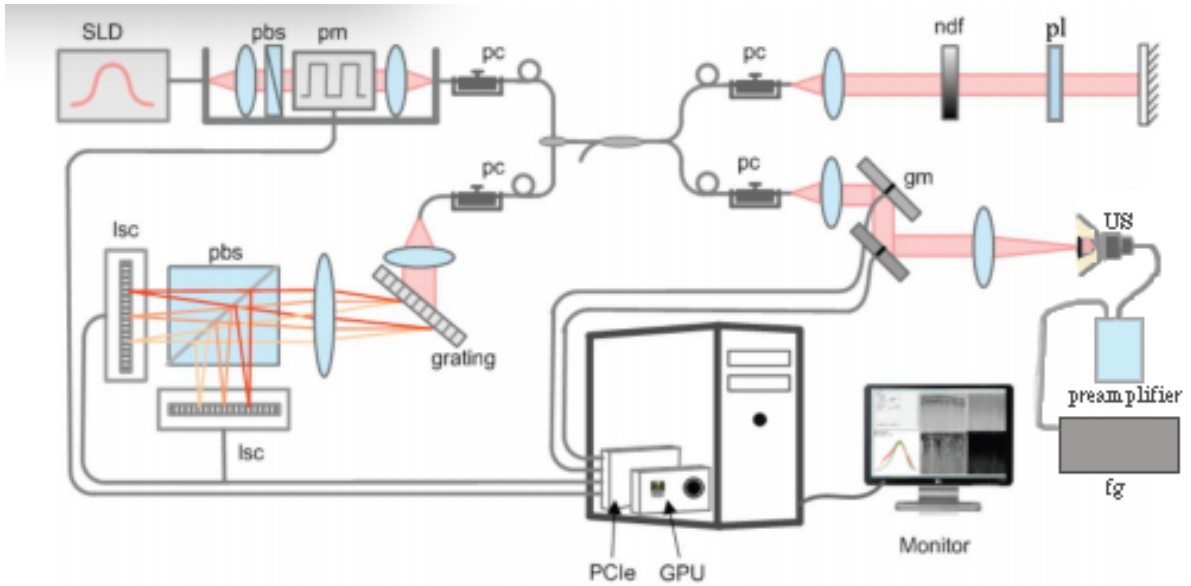
Xeon W5580.



**Figure 1:** Schematic of MF-SD-OCT System with GPU Assisted Processing.

## 6.2 SYSTEM CHARACTERIZATION

Basic system characterization was done in a similar fashion to that of Wang et al and is

seen in Table 2 [20].

**Table 2:** OCT System Characterization;

| | |
|---|---|
| **Power incident on the sample surface** | **6 mW** |
| **Photon-to-electron Conversion Efficiency of Spectrometer** | 64% |
| **Measured Imaging Depth in Air** | 2.95 mm (5.76 microns per pixel) |
| **Measured Imaging Depth in Tissue** | 2 mm (3.91 microns per pixel) |
| **SNR Range** | 51–40 dB* |
| **Sensitivity** | 106dB |
| **Sensitivity drop-off** | <6dB from surface to 1.6 mm (Air) |
| **Axial resolution** | 8 microns (depth of 1mm)<br>11 microns (depth of 3mm with mirror) |

*51dB at the surface and 40 dB at 3mm measured with a mirror.

21

## 6.3 PHASE SENSITIVITY

The accuracy and sensitivity of the OCT system to measure the elasticity of tissue is limited by the phase sensitivity of the optical system, which is determined by the OCT system noise floor. It has been shown that phase sensitivity is proportional to the SNR of the system [45]. With average SNR levels below 50dB, the accuracy of the phase changes is limited to 0.00316 radians calculated by the following equation sensitivity can be calculated by:

$$Phase\ Sensistivity = 1/\sqrt{10^{(\frac{SNR}{10})}} \qquad (18)$$

With our current set up, the phase sensitivity was measured using the top and bottom surfaces of a glass slide attenuated by a neutral density filter. The phase difference between the top and bottom of the coverslip was calculated.
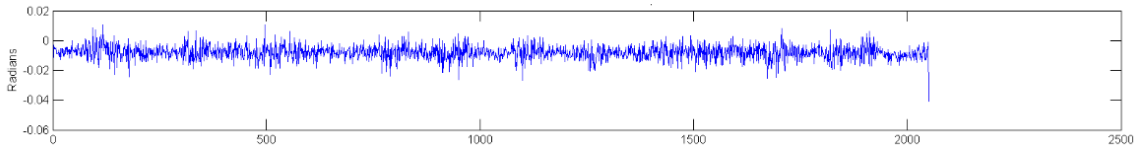


**Figure 2:** Phase Sensitivity over 2048 Measurements.

To covert these changes to the amount of displacement, the following calculation is done.

$$\Delta z = \Delta\phi * (CenterWavelength) * (1/4\pi) \qquad (19)$$

The phase sensitivity was measured to be 0.0041 radians at 48.7dB. The theoretical phase sensitivity at 48.7dB is 0.0037 radians. The differences in the measured values and the theoretical value can be attributed to the environmental vibrations. The minimum resolvable deformation in tissue for the current system is 423 picometers over 2048

measurements. Additionally, the minimum resolvable velocity is 4.23 nm/s and strain rate of $4.23 \times 10^{-4}$%/s with $\Delta t = 100$ ms and assuming the tissue to be 1 mm.

## 6.4 ULTRASOUND INDUCED JITTER

During the finite acquisition time, the spectrum of the OCT modulation will decrease in amplitude by a certain amount due to an US-induced jitter. As the ultrasound frequency increases, the amount of destructive interference of the OCT signal increases as the sample vibrates more amplitude increases. To visualize the variations in amplitude of the spectrum, the difference between the spectrums when the ultrasound is on versus when the ultrasound is off is taken and subtle amplitude changes of the ultrasound jitter is captured. By looking at the standard deviation of the spectrum, the amount of destructive interference can be measured.
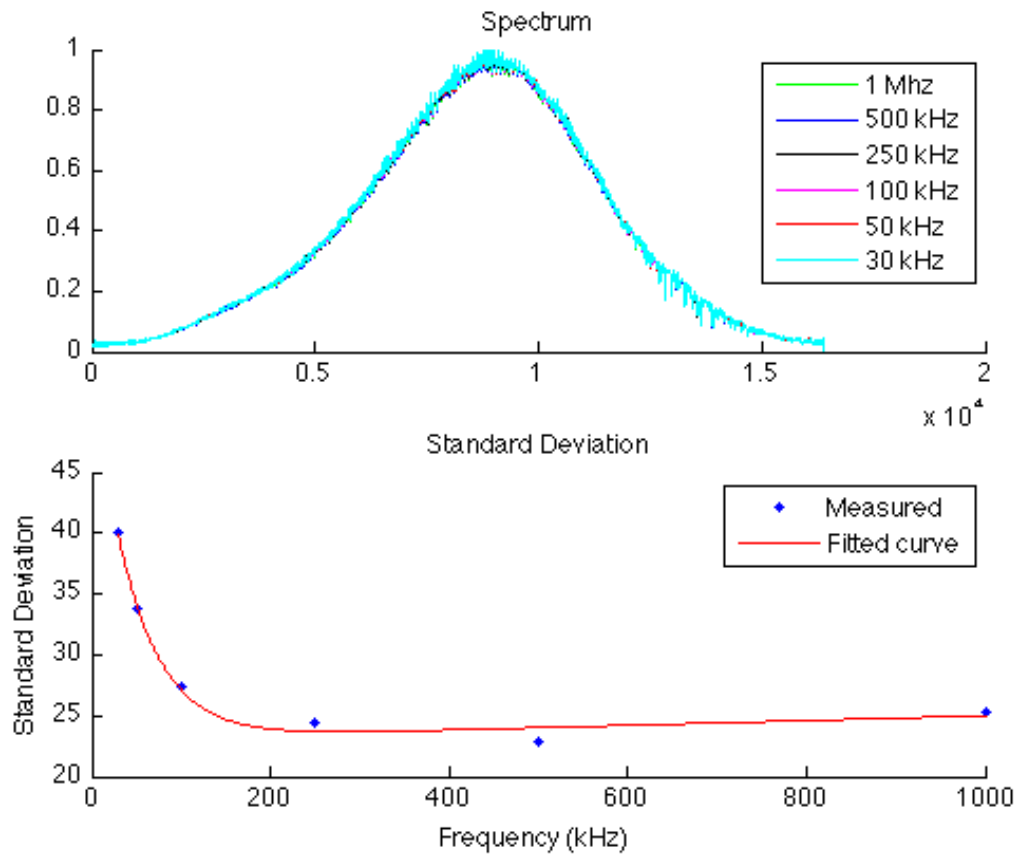
**Figure 3:** Modulation Changes with Ultrasound. *Top:* Normalized Spectrum. *Bottom:* Fitted Standard Deviation of Spectrum

The amount of deconstructive interference across all frequencies was fitted to the following model shown in equation 20 below.

$$f(x) = a * \exp(b * x) + c * \exp(d * x) \qquad (20)$$

*Coefficients* (with 95% confidence bounds):

a = 31.29  (11.43, 51.16)

b = -0.02088  (-0.04141, -0.0003515)

c =  23.07  (17.16, 28.98)

d = 8.044e-05  (-0.000289, 0.0004499)

*Goodness of fit*:

SSE: 2.345

R-square: 0.9893

Adjusted R-square: 0.9733

RMSE: 1.083



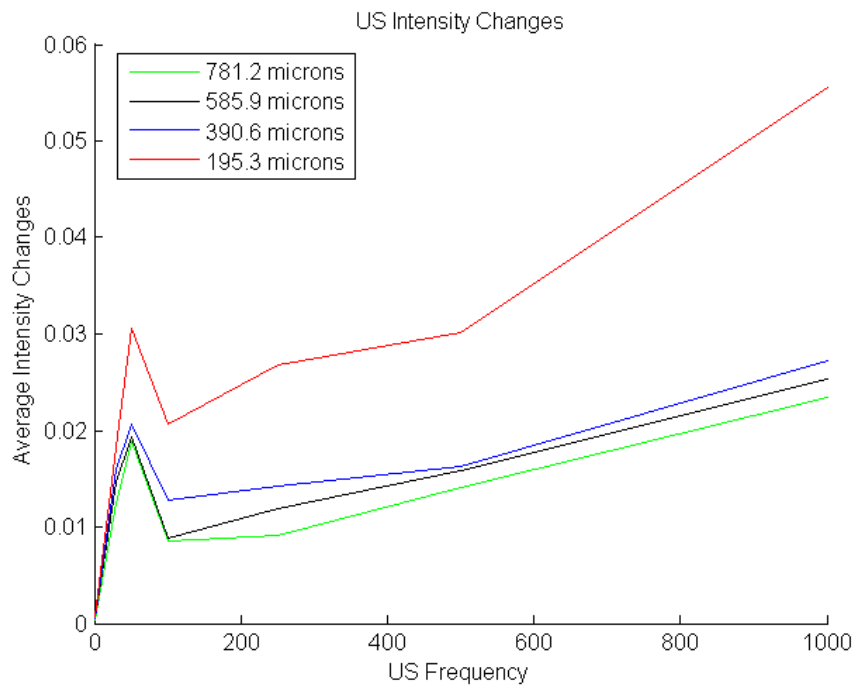**Figure 4:** Intensity Changes with Depth

| 30kHz | 50 kHz | 100 kHz | 250 kHz | 500 kHz | 1000 kHz |
|---|---|---|---|---|---|
| 0.183 | 0.0306 | 0.0206 | 0.0268 | 0.0302 | 0.0555 |
| 0.0159 | 0.0206 | 0.0128 | 0.0143 | 0.0162 | 0.0273 |
| 0.0147 | 0.0194 | 0.0088 | 0.0119 | 0.0158 | 0.0253 |
| 0.0125 | 0.0188 | 0.0086 | 0.0091 | 0.0141 | 0.0235 |

**Table 3:** Average Intensity Changes with Depth

The amount of deconstructive interference is correlated with depth as see in Figure 4. Moving down at increments of 50 pixels or ~200 micrometer in depth the intensity changes minimally at each level. The peak at 50 kHz is related to the 30 kHz acquisition speed of the camera. The intensity changes increase to a threshold before the ultrasound induced vibrations move too quickly for the line scan camera to detect.

## 6.5 CONTROL EXPERIMENTS

A coverslip embedded in gelatin was imaged as the ultrasound was pulsed at 30kHz and 500 kHz. The phase difference between the top and bottom of the coverslip was used to measure the displacement, velocity, and strain rates induced by the ultrasound pressure wave. Nanometer displacements were measured.
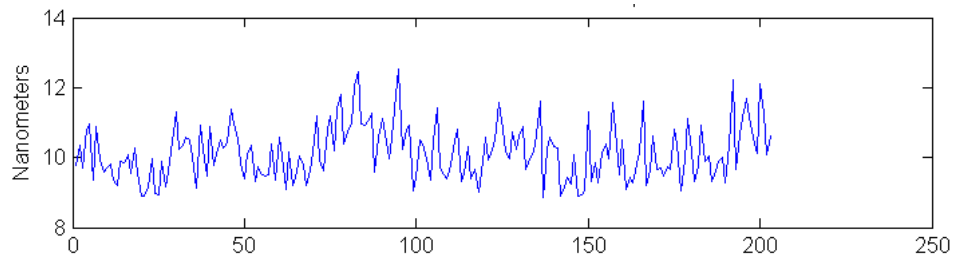


**Figure 5:** Coverslip experiment at 30kHz. Ultrasound was turned on at frame 60.

At an acquisition rate of 30,000 Hz, each measurement equates to 33.3μs and each frame is 68.2 milliseconds. The coverslip thickness is 0.17mm. The average displacements are 2 nm per frame gives a velocity of ~29.3 nm/s and a strain rate of 1.73E05%/s.
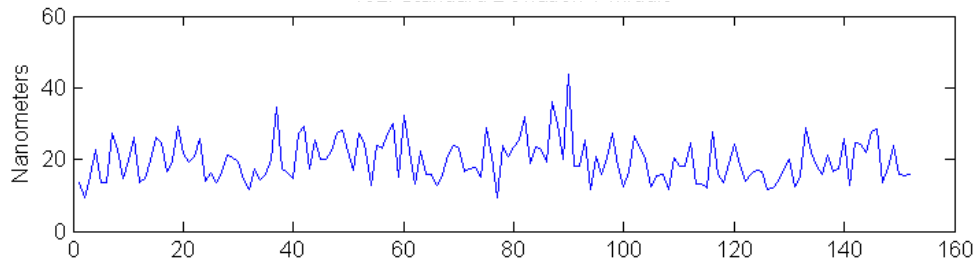
**Figure 6:** Coverslip experiment at 500 kHz. Ultrasound on at frames 2-25; 35-60; 75-95

At an acquisition rate of 30,000 Hz, each measurement equates to 33.3μs and each frame is 68.2 milliseconds. The coverslip thickness is 0.17mm. The average displacements are 20 nm per frame gives a velocity of ~293.2 nm/s and a strain rate of 1.73E06 %/s.

## 7. ANIMAL MODEL & PREPARATION

Osteoarthritis was induced into the right knee of 12 week old female Sprague-Dawley rats via single intraarticular injection using monosodium idoacetate (2 mg in 50 μL saline per knee) (Sigma Aldrich) after anesthetized with isoflurane (Phoenix). The well-established model of Monoiodoacetate-Induced Arthritis (MIA) was used, which yielded pathologies similar to those described by Guzman et al [34]. Typically, MIA knees show close to grade 1 cartilage damage on the condylar surface on day 5, close to grade 2 damage on condyles by day 9 and close to grade 3-3.5 cartilage and bone damage on day 21, following the grading system described by Pritzker et al [35].

Sham controls were injected with 50 μL 0.9% saline into the right knee. OA-induced rats were sacrificed on day 5, 8, and 11. Sham controls were sacrificed on day 15. Rats were

euthanized by $CO_2$ inhalation followed by cervical dislocation. The femur and tibia of both legs (OA-induced and control) were extracted [36].

All protocols were approved by the Institutional Animal Care and Use Committee at UCR.
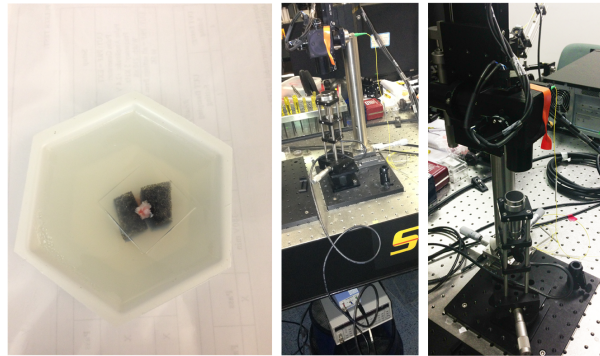
# 8. EXPERIMENTAL DESIGN



**Figure 7:** *Left:* Sample preparation embedding in gelatin with coverslip placed on top. *Middle:* Ultrasound connected to preamplifier and function generator. *Right:* OCT sample arm + close up of ultrasound and stage.

Osteoarthritis was induced into the right knee of 12 week old female Sprague-Dawley rats via single intraarticular injection using monosodium idoacetate (2 mg in 50 µL saline per knee) (Sigma Aldrich) after anesthetized with isoflurane (Phoenix). Sham controls were injected with 50 µL 0.9% saline into the right knee. OA-induced rats were sacrificed on day 5, 8, and 11. Sham controls were sacrificed on day 15. Rats were euthanized by $CO_2$ inhalation followed by cervical dislocation. The femur and tibia of both legs (OA-induced and control) were extracted [34]. On days 5, 8, 11, and 15, PS-OCT is used to image the micro-volumes of femur and tibia cartilage to obtain structural

information and distinguish layers in cartilage. The femur and tibia is then embedded in

cartilage in gelatin with a coverslip place over cartilage for a phase reference and imaged

with OCT as an external pressure wave is sent by the ultrasound transducer (Olympus

Parametrics NDT V318 Transducer) and preamplifier (Olympus Parametrics

Preamplifier 5660B) reflected off the coverslip* onto the surface of the cartilage. Bone

samples then are fixed in 10% formalin (Fisher Scientific) after which they were

decalcified using EDTA. Following decalcification the samples underwent histological

processing and were stained with Masson's trichrome to detect structural abnormalities.

The software programs, MATLAB and Amira, were used to process the data.

# 9. RESULTS & DISCUSSION

## 9.1 STRUCTURAL COMPARISON OF PS-OCT & HISTOLOGY

PS-OCT provides additional contrast over traditional OCT images as seen in Figure 6. From the traditional OCT images, the different layers of cartilage cannot be seen (Figure 6 – left); however, with PS-OCT the different layers of articular cartilage up to the deep zone can be seen. This is due to the different orientation of the collagen fibril network in each layer. The layer order is as follows: superficial, middle zone, deep zone, calcified cartilage.
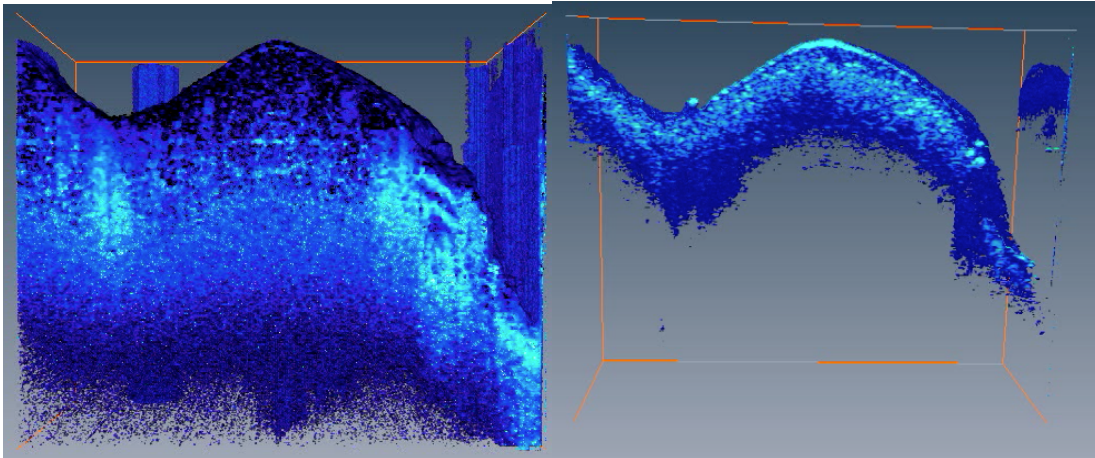


**Figure 8**: OCT vs PS-OCT in a blue false color map.

**Figure 9***: **A**: PS-OCT Image of Femur. **B**: Depth Profile and Linear Regression fit overlaid onto of region of femur cartilage. **C**: Depth Profile and Linear Regression fit corresponding to 3 layers of 39.1 (Red), 27.4 (Blue), and 139.9 (Green) microns thickness and an exponential fit, r-squared value of 0.9895.
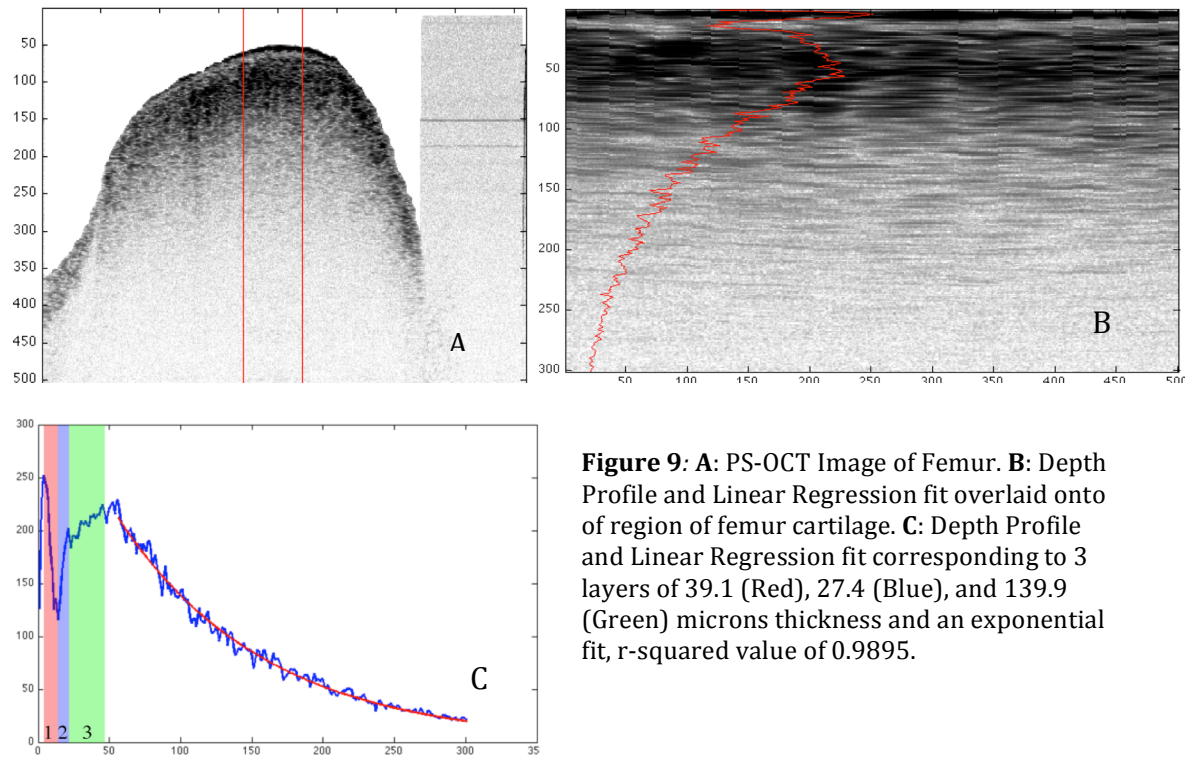
Figure 9a shows a PS-OCT Image of a rat femur. The different layers of cartilage are distinguishable and can be quantified with a depth profile and linear regression fit seen in Figures 9b and 9c. The superficial zone was calculated to be 39.1 microns, the middle zone was calculated to be 27.4 microns, and the deep zone was calculated to be 139.9 micrometers. The last and subchrondral bone cannot be seen or characterized for certainty as the OCT signal drops offs. The sizes correlate well with the average cartilage thickness between 200-300 microns.
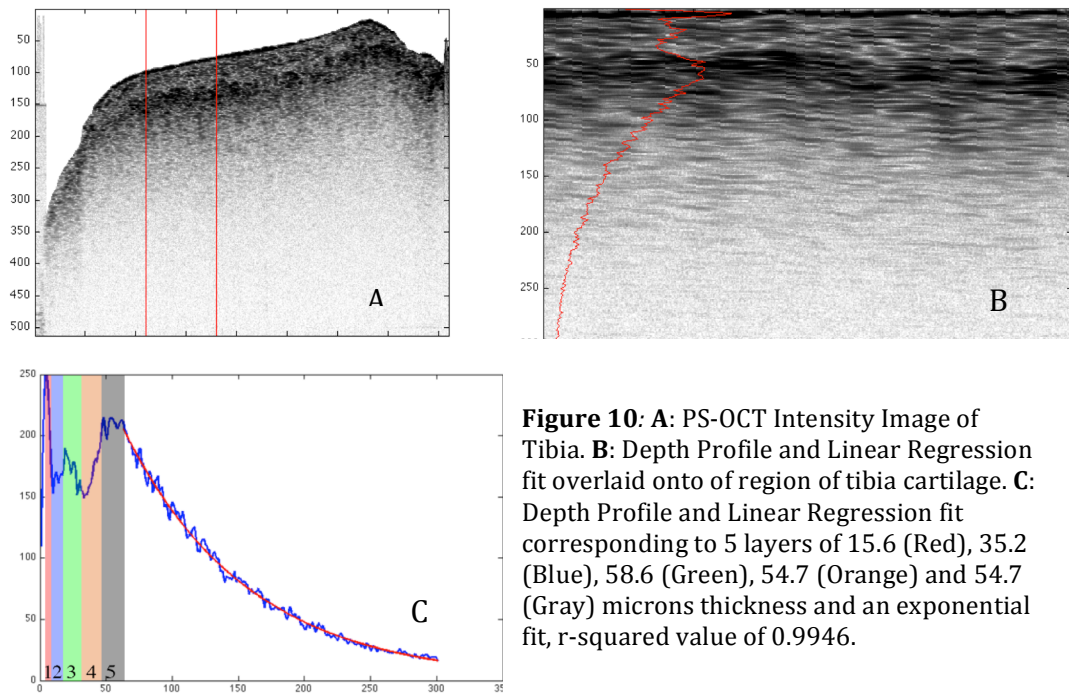
**Figure 10**: **A**: PS-OCT Intensity Image of Tibia. **B**: Depth Profile and Linear Regression fit overlaid onto of region of tibia cartilage. **C**: Depth Profile and Linear Regression fit corresponding to 5 layers of 15.6 (Red), 35.2 (Blue), 58.6 (Green), 54.7 (Orange) and 54.7 (Gray) microns thickness and an exponential fit, r-squared value of 0.9946.

Figure 10a shows a PS-OCT Image of a rat femur. The different layers of cartilage are distinguishable and can be quantified with a depth profile and linear regression fit seen in Figure 10b and 10c. The superficial zone was calculated to be 15.6 microns, the middle zone was calculated to be 35.2 microns, and the deep zone was calculated to be 58.6 micrometers. The calcified cartilage was found to be 54.7 and subchrondral bone signal went to 54.7 microns before the OCT signal drops off.

## 9.2 PS-OCT STUDY OF OA PROGRESSION

For this study, PS-OCT image sections were taken of monoiodacetate-induced arthritis rat cartilage to validate the capabilities of PS-OCT to distinguish the micrometer level layers of cartilage. 1mm x 1mm sections were imaged on the medial and lateral sides along the condyles ridge and patellar groove. 2-D Cross sectional images of the cartilage were processed by MATLAB and viewed in 3-D by Amira. Intensity and polarization sensitive images were generated.
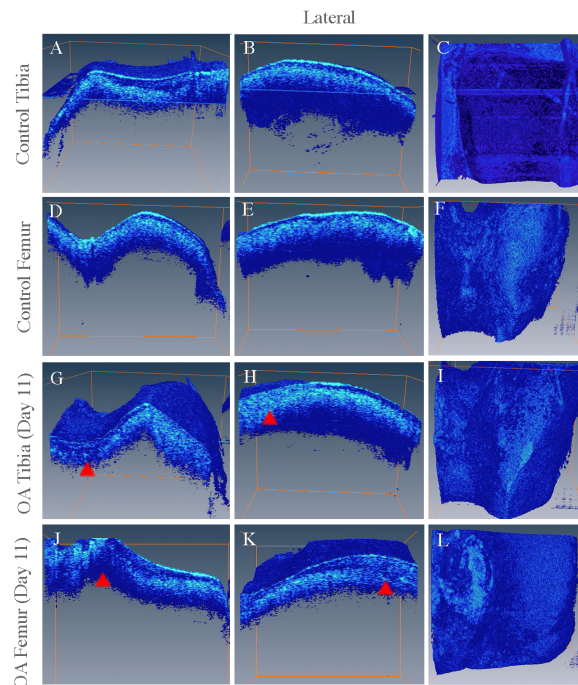


**Figure 11**: PS-OCT Images of Day 5 of OA disease progression in lateral section of rat femur and tibia. *Leftmost:* Coronal Plane View. *Middle:* Sagittal Plane View. *Rightmost:* Transverse Plane View. *A-C:* Control Tibia. *D-F:* Control Femur. *G-I:* OA Tibia *J-L:* OA Femur

For day 5 of the OA disease progression study, the control volumes showed distinct layers of articular cartilage. However, small sections of the cartilage show a loss layered structure. The banding of the three different layers of cartilage slowly dissipates for a

33

third of the OCT volume section in figure 11H. This is also seen in the coronal and

sagittal view in figure 11J and 11K. In figure 11J, the layer banding becomes less distinct

along the ridge of the femoral condyle. In figure 11K, the sagittal view also shows a

lessening of the layered structure indicating a possible degradation of collagen fibril

network in that area. The transverse view shows no significant changes to the surface of
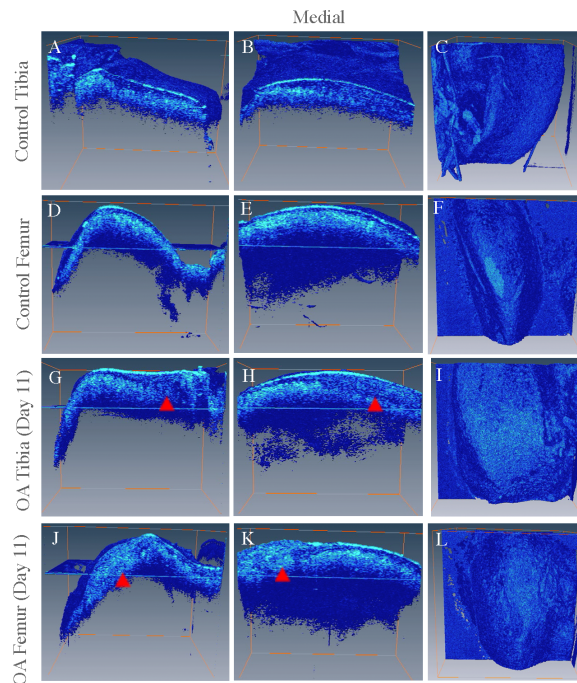
the cartilage.



**Figure 12:** PS-OCT Images of Day 5 of OA disease progression in medial section of rat femur and tibia. *Leftmost:* Coronal Plane View. *Middle:* Sagittal Plane View. *Rightmost:* Transverse Plane View. *A-C:* Control Tibia. *D-F:* Control Femur. *G-I:* OA Tibia *J-L:* OA Femur

Along the medial side, the controls maintain the distinct layering while the OA femur and

tibia lose distinction in the middle and deep zones seen in the sagittal plane view in

figures 12H, 12K. No surface changes are distinguishable in the transverse view of all
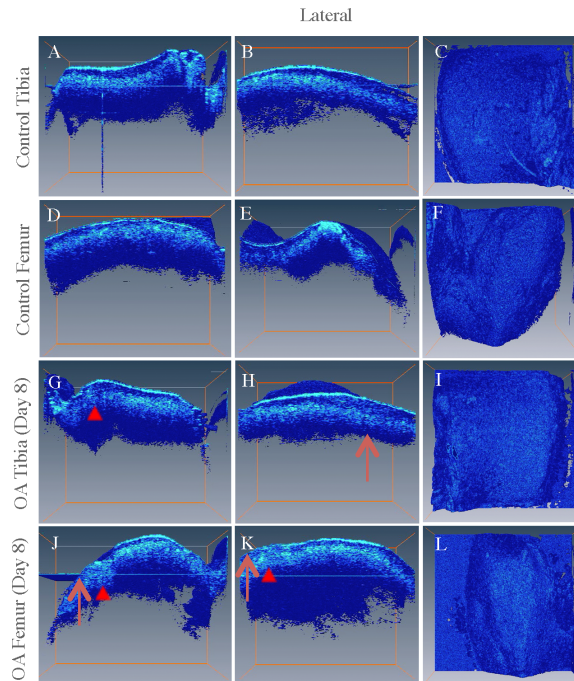
samples.

**Figure 13:** PS-OCT Images of Day 8 of OA disease progression in lateral section of rat femur and tibia. *Leftmost:* Coronal Plane View. *Middle:* Sagittal Plane View. *Rightmost:* Transverse Plane View *A-C: Control Tibia. D-F: Control Femur. G-I:* OA Tibia *J-L:* OA Femur

On day 8 of the disease progression, as expected the control volumes maintain the 3 layer banding integrity. However as with day 5, small sections of the cartilage show a loss in its layered structure. This is also seen in the coronal and sagittal view in figure 13H, 13J and 13K. The distinction between the middle and deep zone lessens in figure 13H. In figure 13K, the layer banding becomes less distinct along the ridge of the femoral condyle. In figure 13K, the sagittal view also shows a lessening of the layered structure indicating a possible degradation of collagen fibril network in that area. The banding of the three different layers of cartilage slowly dissipates for a quarter of the OCT volume section in figure 13K. The transverse view displays no surface damage.
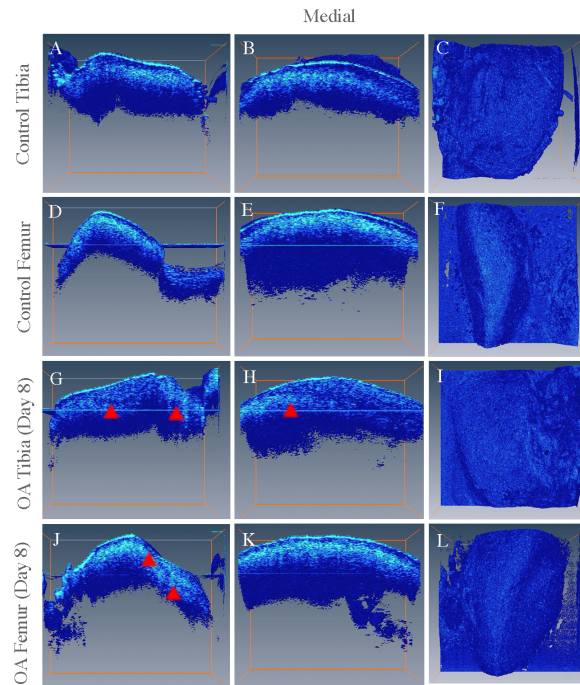
**Figure 14:** PS-OCT Images of Day 8 of OA disease progression in medial section of rat femur and tibia. *Leftmost:* Coronal Plane View. *Middle:* Sagittal Plane View. *Rightmost:* Transverse Plane View. *A-C: Control Tibia. D-F: Control Femur. G-I: OA Tibia J-L:* OA Femur

Similarly for the medial side in day 8 of OA disease progression, the deep zones and middle zones are now almost completely homogenous in the OA Tibia seen in figures 14G and 14H, but the OA femur seems to be unaffected. No significant surface deformations were seen.
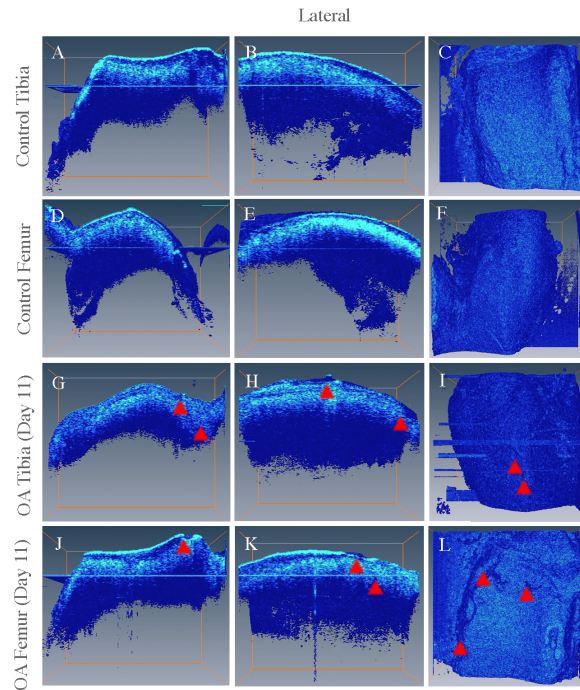
**Figure 15:** PS-OCT Images of Day 11 of OA disease progression in lateral section of rat femur and tibia. *Leftmost:* Coronal View. *Middle:* Sagittal Plane View. *Rightmost:* Transverse Plane View. *A-C:* Control Tibia. *D-F:* Control Femur. *G-I:* OA Tibia *J-L:* OA Femur

In day 11 of the study, the controls maintain the layered structure of cartilage while the OA induced femur and cartilage partially lose their birefringent properties cause by the distinct organization of collagen fibril network in cartilage seen in figures 15G, 15H, 15J, and 15K. Surface deformation can be seen in the transverse views for the OA femur and tibia as well as in figure 15H.
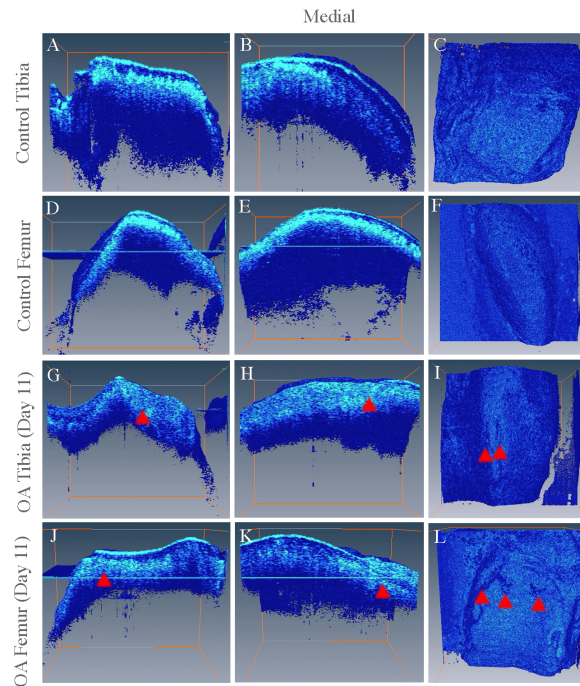
**Figure 16:** PS-OCT Images of Day 11 of OA disease progression in medial section of rat femur and tibia. *Leftmost:* Coronal Plane View. *Middle:* Sagittal Plane View. *Rightmost:* Transverse Plane View. *A-C:* Control Tibia. *D-F:* Control Femur. *G-I:* OA Tibia *J-L:* OA Femur

In the OA tibia on the medial side, the layers completely dissipate while in the OA femur only the deep and middle zones seem to be affected seen in figures 16G, 16H, 16J, and 16K, respectively. There are no changes in banding in the controls.
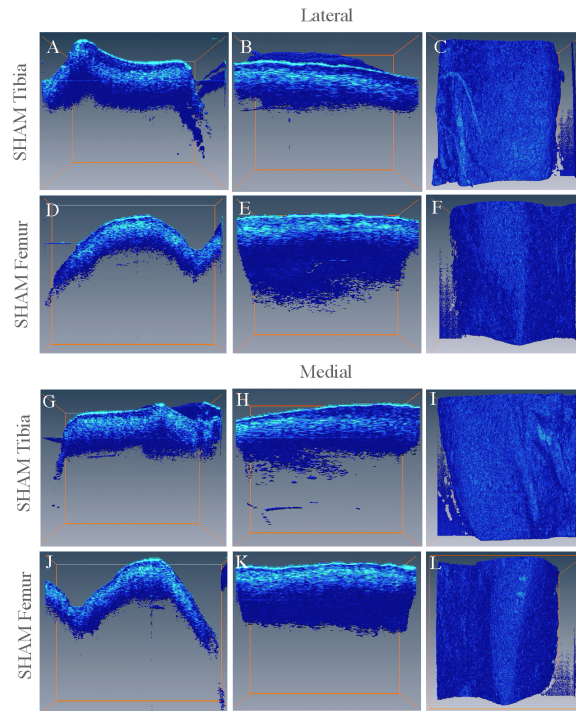
**Figure 17:** PS-OCT Images of SHAM Control of OA disease progression in lateral and medial sections of rat femur and tibia. *Leftmost:* Coronal Plane View. *Middle:* Sagittal Plane View. *Rightmost:* Transverse Plane View. *A-C:* Control Tibia. *D-F:* Control Femur. *G-I:* OA Tibia *J-L:* OA Femur

For the SHAM control, no significant changes in the cartilage layer structure are seen.
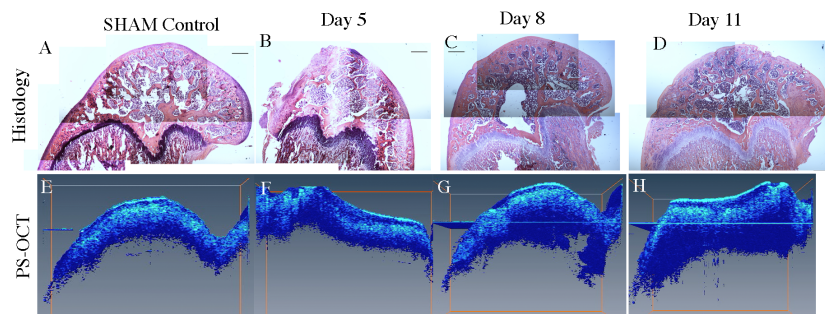


**Figure 18:** PS-OCT comparison with histology. Histology scale bar = 100 microns

PS-OCT is able to distinguish the superficial, middle layer and deep zone of the rat articular cartilage. In conclusion, PS-OCT was able to detect changes in the deep and middle zone as early day 5. 3D PS-OCT is advantageous in it ability to quickly slice through the volume areas in all different planes to visualize the OA affected area seen by

the degradation of the collagen fibril network. Although PS-OCT cannot diagnosis the disease for certain it can be extremely useful in detecting the areas to perform elastography for a PS-OCT guided elastography method for detecting OA.
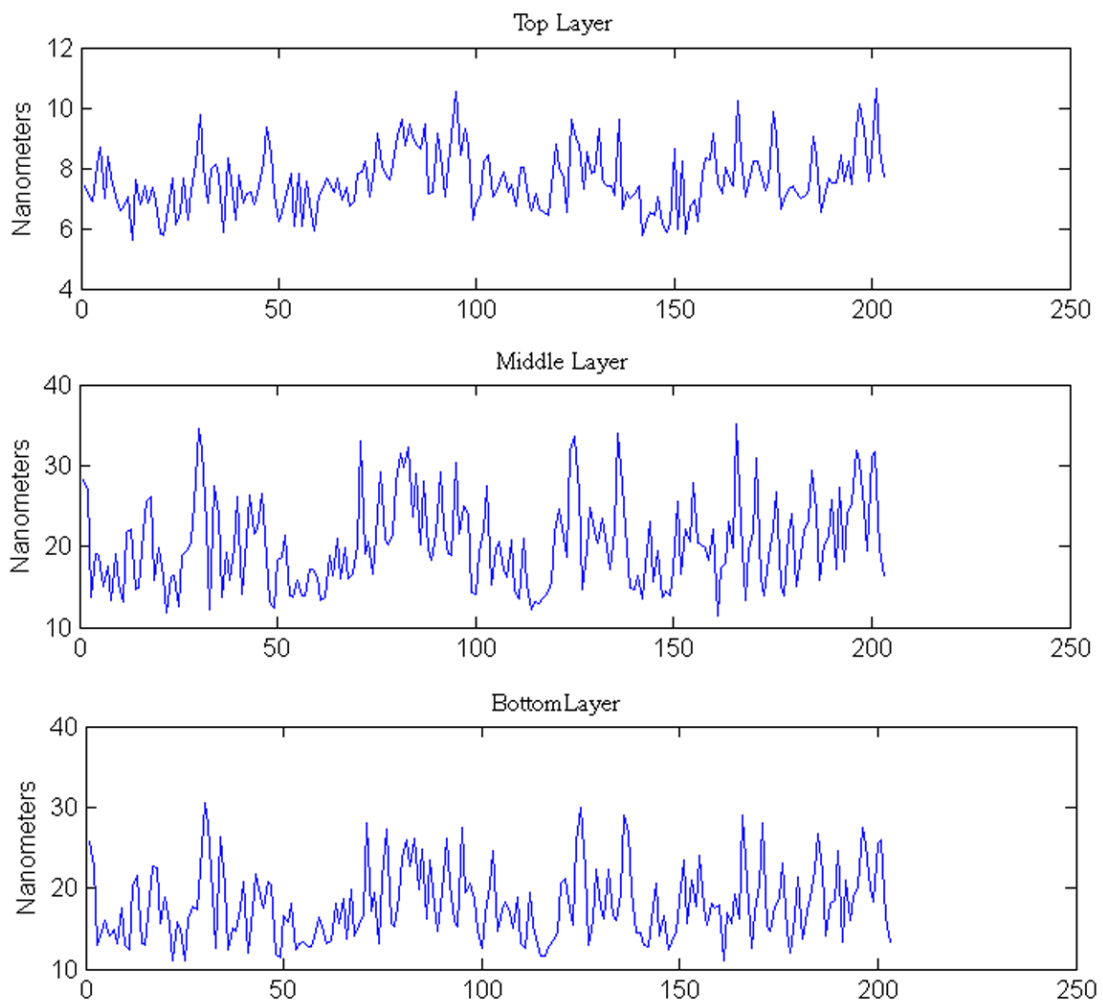
## 9.4 ANIMAL EXPERIMENTS



**Figure 19:** Layer Specific Rat Femur Experiment. Ultrasound on at frames 30-50, 75-100, 120-140, 160-202.

At an acquisition rate of 30,000 Hz, each measurement equates to 33.3μs and each frame is 68.2 milliseconds. Assuming the superficial cartilage layer thickness is 39.1 microns, the average displacement is ~3 nm, which corresponds to a velocity of ~44 nm/s and strain rate of 1.13E06 %/s. Given that the middle layer thickness is 27.4 micron and the deep zone layer thickness is 139.9 microns, the average displacements are the same for the second and third layers at ~15 nm per frame gives a velocity of 219.9 nm/s and a strain rate of 8.02E06 %/s and 1.57E06 %/s for the second and third layer, respectively.
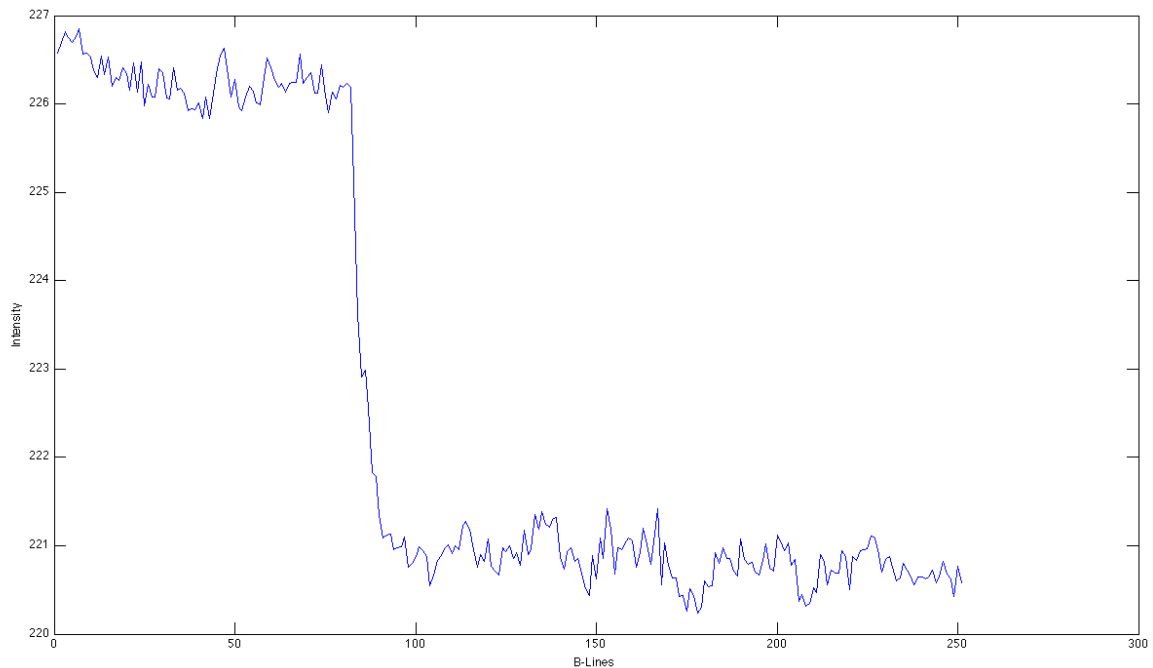


**Figure 20:** Femoral Intensity Changes. Ultrasound on at frames 85.

A region of interest area of 1801 pixels was selected and averaged over time to show the relative intensity changes in the rat femur with and without the ultrasound. For the rat femur, the baseline intensity stabilizes around a relative intensity of 226.5 and significantly drops after the ultrasound is turned on at B-line 85 to a relative intensity of 221. There is a 5.5-drop in relative intensity or a 2.4% drop in intensity.

41

## 10. CONCLUSION

An ultrasound modulation intensity analysis would be ideal in cases where the ultrasound resonant frequency is much greater than the acquisition speed of the camera. Whereas a phase analysis would be the most accurate when the ultrasound resonant frequency is close to the acquisition speed of the camera. A need to characterize the amount of ultrasound periods in a single acquisition line would need to be further investigated. A PS-OCT Guided Elastography method for the early detection of OA would provide information about the relative stiffness of the bulk cartilage matrix at the early stages. It is advantageous in detecting the collagen disorganization early on as the birefringent properties of the matrix change as OA progresses. Additionally, PS-OCT volume sets would be able to pinpoint areas of OA-induced collagen fibril disorganization verses healthy cartilage. Moreover, the elastography measurements would be able to confirm the weakening of the cartilage matrix layer by layer either by measuring the strain rates or the relative intensity changes. For future work, more OA experiments would be needed to show statistical significance and to further confirm this method. In order to have any clinical significance an OA OCT scoring system would be need to be implemented.